The Astrophysical Journal, 970:68 (14pp), 2024 July 20 https://doi.org/10.3847/1538-4357/ad4cea

Efficient NIRCam Selection of Quiescent Galaxies at $3 < z < 6$ in CEERS

Arianna S. Long[1,29], Jacqueline Antwi-Danso[2,3], Erini L. Lambrides[4,30], Christopher C. Lovell[5,6], Alexander de la Vega[7], Francesco Valentino[8,9,10], Jorge A. Zavala[11], Caitlin M. Casey[1], Stephen M. Wilkins[12,13], L. Y. Aaron Yung[14,30], Pablo Arrabal Haro[15], Micaela B. Bagley[1], Laura Bisigello[16,17], Katherine Chworowsky[1,31], M. C. Cooper[18], Olivia R. Cooper[1,31], Asantha R. Cooray[18], Darren Croton[19,20], Mark Dickinson[15], Steven L. Finkelstein[1], Maximilien Franco[1], Katriona M. L. Gould[8,9], Michaela Hirschmann[21], Taylor A. Hutchison[14,30], Jeyhan S. Kartaltepe[22], Dale D. Kocevski[23], Anton M. Koekemoer[24], Ray A. Lucas[24], Jed McKinney[1], Rachel Nere[25], Casey Papovich[2,3], Pablo G. Pérez-González[26], Nor Pirzkal[27], and Paola Santini[28]

[1] Department of Astronomy, The University of Texas at Austin, Austin, TX, USA; arianna.sage.long@gmail.com
[2] George P. and Cynthia Woods Mitchell Institute for Fundamental Physics and Astronomy, Texas A&M University, College Station, TX 77843-4242, USA
[3] Department of Physics and Astronomy, Texas A&M University, College Station, TX 77843-4242, USA
[4] NASA-Goddard Space Flight Center, Code 662, Greenbelt, MD 20771, USA
[5] Institute of Cosmology and Gravitation, University of Portsmouth, Burnaby Road, Portsmouth PO1 3FX, UK
[6] Centre for Astrophysics Research, School of Physics, Engineering & Computer Science, University of Hertfordshire, Hatfield AL10 9AB, UK
[7] Department of Physics and Astronomy, University of California, 900 University Avenue, Riverside, CA 92521, USA
[8] Cosmic Dawn Center (DAWN), Denmark
[9] Niels Bohr Institute, University of Copenhagen, Jagtvej 128, DK-2200 Copenhagen N, Denmark
[10] European Southern Observatory, Karl-Schwarzschild-Str. 2, D-85748 Garching bei Munchen, Germany
[11] National Astronomical Observatory of Japan, 2-21-1 Osawa, Mitaka, Tokyo 181-8588, Japan
[12] Astronomy Centre, University of Sussex, Falmer, Brighton BN1 9QH, UK
[13] Institute of Space Sciences and Astronomy, University of Malta, Msida MSD 2080, Malta
[14] Astrophysics Science Division, NASA Goddard Space Flight Center, 8800 Greenbelt Road, Greenbelt, MD 20771, USA
[15] NSF's National Optical-Infrared Astronomy Research Laboratory, 950 N. Cherry Avenue, Tucson, AZ 85719, USA
[16] Dipartimento di Fisica e Astronomia "G.Galilei", Universitá di Padova, Via Marzolo 8, I-35131 Padova, Italy
[17] INAF–Osservatorio Astronomico di Padova, Vicolo dell'Osservatorio 5, I-35122 Padova, Italy
[18] Department of Physics & Astronomy, University of California, Irvine, 4129 Reines Hall, Irvine, CA 92697, USA
[19] Centre for Astrophysics & Supercomputing, Swinburne University of Technology, Hawthorn, VIC 3122, Australia
[20] ARC Centre of Excellence for All Sky Astrophysics in 3 Dimensions (ASTRO 3D), Australia
[21] Institute of Physics, Laboratory of Galaxy Evolution, Ecole Polytechnique Fédérale de Lausanne (EPFL), Observatoire de Sauverny, 1290 Versoix, Switzerland
[22] Laboratory for Multiwavelength Astrophysics, School of Physics and Astronomy, Rochester Institute of Technology, 84 Lomb Memorial Drive, Rochester, NY 14623, USA
[23] Department of Physics and Astronomy, Colby College, Waterville, ME 04901, USA
[24] Space Telescope Science Institute, 3700 San Martin Drive, Baltimore, MD 21218, USA
[25] The School of Physics, Georgia Institute of Technology, Atlanta, GA, USA
[26] Centro de Astrobiología (CAB), CSIC-INTA, Ctra. de Ajalvir km 4, Torrejón de Ardoz, E-28850 Madrid, Spain
[27] ESA/AURA Space Telescope Science Institute, USA
[28] INAF—Osservatorio Astronomico di Roma, via di Frascati 33, 00078 Monte Porzio Catone, Italy

Received 2023 June 7; revised 2024 May 7; accepted 2024 May 14; published 2024 July 17

Abstract

Substantial populations of massive quiescent galaxies at $z \geqslant 3$ challenge our understanding of rapid galaxy growth and quenching over short timescales. In order to piece together this evolutionary puzzle, more statistical samples of these objects are required. Established techniques for identifying massive quiescent galaxies are increasingly inefficient and unconstrained at $z > 3$. As a result, studies report that as much as 70% of quiescent galaxies at $z > 3$ may be missed from existing surveys. In this work, we propose a new empirical color selection technique designed to select massive quiescent galaxies at $3 \lesssim z \lesssim 6$ using JWST NIRCam imaging data. We use empirically constrained galaxy spectral energy distribution (SED) templates to define a region in the F277W − F444W versus F150W − F277W color plane that captures quiescent galaxies at $z > 3$. We apply these color selection criteria to the Cosmic Evolution Early Release Science (CEERS) Survey and use SED fitting on sources in the region to identify 44 candidate $z \gtrsim 3$ quiescent galaxies. Over half of these sources are newly discovered and, on average, exhibit specific star formation rates of poststarburst galaxies. Most of these sources would not be discovered using canonical *UVJ* diagrams. We derive volume density estimates of $n \sim 1\text{–}4 \times 10^{-5}$ Mpc^{-3} at $3 < z < 5$, finding excellent agreement with existing reports on similar populations in the CEERS field. Thanks to NIRCam's wavelength coverage and sensitivity, this technique provides an efficient tool to search for large samples of these rare galaxies.

---

[29] NASA Hubble Fellow.
[30] NASA Postdoctoral Fellow.
[31] NSF Graduate Fellow.

Unified Astronomy Thesaurus concepts: Quenched galaxies (2016); High-redshift galaxies (734); Two-color diagrams (1724)

1. Introduction

One of the most puzzling discoveries in galaxy evolution of the decade is that substantial populations of massive galaxies ($M_* \gtrsim 10^{10.5}\ M_\odot$) ceased forming stars as early as two billion years after the Big Bang ($z > 3$; Toft et al. 2014; Glazebrook et al. 2017; Merlin et al. 2019; Shahidi et al. 2020; Valentino et al. 2020; Forrest et al. 2020; Carnall et al. 2023). Many of the best available cosmological models struggle to produce adequate populations—if any at all—of massive quiescent galaxies at $z > 3$ (Steinhardt et al. 2016; Schreiber et al. 2018; Cecchi et al. 2019, see also EAGLE in Merlin et al. 2019; FLARES in Lovell et al. 2023), highlighting our incomplete understanding of the physics required to quench these behemoths over the short periods of time available in the early cosmos. Recent discoveries of surprisingly massive star-forming galaxies at $z > 6$ apply even further pressure on our understanding of cosmology and galaxy quenching physics (Boylan-Kolchin 2023; Lovell et al. 2023; Robertson et al. 2023) as these galaxies must form and quench in $\lesssim$1 Gyr to match observations at later times. Therefore, identifying and characterizing large samples of early massive quiescent galaxies is fundamental to testing our theories on the construction of the first massive galaxies.

In order to understand the formation of massive quiescent galaxies in the $z > 3$ cosmos, we must first securely identify statistical samples of these extreme objects. Quiescent galaxies at $z > 3$ are exceedingly rare ($n \sim 10^{-5}$–10^{-6} Mpc^{-3}; Girelli et al. 2019; Santini et al. 2019; Shahidi et al. 2020; Valentino et al. 2020; Carnall et al. 2023; Long et al. 2023), making their identification a strenuous process. Over the last two decades, identification techniques for quiescent galaxies were established primarily through rest-frame color–color diagrams. The majority of color selection techniques for these objects use a galaxy's rest-frame *J*-band magnitude to distinguish between dust-reddened star-forming galaxies and quiescent galaxies (see e.g., the *UVJ* diagram; Labbé et al. 2005; Williams et al. 2009; Brammer et al. 2011; Belli et al. 2019). However, at $z > 3$ the rest-frame *J*-band redshifts to wavelengths $> 5\ \mu$m, falling into a spectral window that typically has no direct observational constraints (and if there are constraints through, e.g., Spitzer IRAC data, it is often too shallow to reliably detect these galaxies). In these cases, studies instead interpolate the rest-frame *J*-band magnitude from an unconstrained portion of the galaxy's spectral energy distribution (SED), and are therefore model dependent. The MIRI instrument on JWST, with imaging coverage between $\lambda \approx 6$–$25\ \mu$m, could aid in rest-frame *J*-band measurements at $z > 3$, however it has a much smaller on-sky footprint for the majority of JWST Cycle 1 legacy surveys currently underway (e.g., only a single band of MIRI imaging is scheduled to cover $\sim$35% of the widest Cycle 1 JWST survey, COSMOS-Web; Casey et al. 2023). Given the rarity of $z > 3$ quiescent galaxies, such a lack of coverage is a severe challenge for methods that employ rest-frame *J*-band magnitudes in high-*z* quiescent galaxy searches.

Another major problem with current color selection methods is that they are tuned to the $z < 2$ Universe, where there is a strong color bimodality in the quiescent versus star-forming galaxy populations (Labbé et al. 2005; Williams et al. 2009; Brammer et al. 2011). At $z > 3$, this bimodality is significantly less distinct (Whitaker et al. 2011; Muzzin et al. 2013; Straatman et al. 2016) as many quiescent galaxies at high-*z* exhibit young ages (<500 Myr), making them appear bluer than typical quiescent galaxies at $z < 3$ (Forrest et al. 2020; D'Eugenio et al. 2020a; Stevans et al. 2021; Pérez-González et al. 2023). This is likely because not enough time has passed to allow for their stellar populations to fully age and redden to match the colors of quiescent galaxies at $z < 2$ (Merlin et al. 2018; Lovell et al. 2023). Depending on the method, this can result in catastrophic losses of sample completeness, whereas much as $\sim$70% of quiescent galaxies at these epochs could be entirely missed (Deshmukh et al. 2018; Merlin et al. 2018; Valentino et al. 2020; Lovell et al. 2023). Furthermore, the rest-frame colors of galaxies with heavily dust-reddened stellar spectra can masquerade as quiescent galaxy colors in the $z > 1$ cosmos (Hwang et al. 2021; Deshmukh et al. 2018; Martis et al. 2019) and, depending on the epoch, dust-obscured galaxies may have similar population densities (Toft et al. 2014; Simpson et al. 2014; Long et al. 2023). These degeneracies yield significant rates (10%–40%) of false positives in the hunt for quiescent galaxies at high-*z*.

This work aims to provide an efficient way to identify $z > 3$ quiescent galaxy candidates using only JWST NIRCam photometry. With its unprecedented combination of sensitivity, resolution, and field of view, JWST will discover and characterize more $z > 3$ quiescent galaxies than ever before (and has already demonstrated that promise; e.g., Carnall et al. 2023; Valentino et al. 2023). In order to take advantage of this new observational era, new techniques must be developed to efficiently select quiescent galaxies at $z > 3$ using the most widely available and constraining JWST photometry—i.e., NIRCam imaging. In this paper, we propose an empirical color selection technique for the efficient identification of massive quiescent galaxy candidates at $3 < z < 5$. This method uses the F277W − F444W versus F150W − F277W color plane (i.e., three bands of photometry: F150W, F277W, and F444W) to identify the candidate parent population for which we run SED modeling to pull out the most likely quiescent galaxy candidates. Importantly, this method yields more young, poststarburst-like quiescent galaxy candidates than all *UVJ*-based techniques. In addition to its strength in candidate selection, this method is also efficient in that it filters out >99% of sources, thereby immensely reducing the resources typically dedicated to sifting through catalogs for these rare objects. Furthermore, due to the chosen filters that define this color space, this method is applicable to the majority of ongoing and upcoming JWST wide and/or deep surveys, including COSMOS-Web (Casey et al. 2023), Cosmic Evolution Early Release Science (CEERS; Finkelstein et al. 2017; Bagley et al. 2023), JADES (Bunker et al. 2020), PANORAMIC (Williams et al. 2021), and PRIMER (Dunlop et al. 2021).

In Section 2, we describe the observed data used to derive and test the F277W − F444W versus F150W − F277W color space. In Section 3, we present the selection "wedge" and the physical motivation behind the selection criteria. Finally, in Section 4, we present preliminary results from applying the color selection technique to CEERS survey data. Throughout this work, we adopt a Planck cosmology, where $H_0 = 67.7$ km s^{-1} Mpc^{-1} and

$\Omega_\Lambda = 0.692$ (Planck Collaboration et al. 2016); where relevant, we adopt a Chabrier initial mass function (IMF; Chabrier 2003), and all quoted colors/magnitudes are in the AB system.

2. Spectral Energy Distribution Templates

It is difficult, and perhaps currently impossible, to identify a ground-truth reference sample that encapsulates all the diversity in colors of $z > 3$ quiescent galaxies. For example, analogous lower redshift samples—even those with evidence for recent starburst activity—are still dominated by a stellar population that is $\gtrsim$1 Gyr old (see, e.g., Wu et al. 2018; D'Eugenio et al. 2020b), which means their colors will be inherently redder than the young (<500 Myr) sources we seek to identify at $z > 3$. Additionally, samples at $z > 3$ are predominantly identified using their rest-frame *UVJ* colors—which are known to be incomplete in capturing this rare population at these epochs. Still, probing the color space of the empirically constrained, spectroscopically confirmed SEDs of our target population (and potential contaminants) remains the best option, with mock SEDs coming second best. Ultimately, future samples of diverse and spectroscopically confirmed sources will aid in the refinement of this and many other selection techniques.

To determine the locus of $3 < z < 5$ quiescent galaxies, as well as potential contaminant populations, we collate JWST NIRCam colors from a variety of empirically constrained SEDs. The primary set of galaxy SEDs used in this analysis are shown in Figure 1. For the purposes of this work, JWST NIRCam colors are interpolated from these SEDs. Future, more expanded tests on the robustness of this selection technique will benefit from results derived from Cycle 1 and Cycle 2 JWST observations.

2.1. z > 3 *Quiescent Galaxies*

For known $z = 3$–5 quiescent galaxies, we use the SEDs derived in Valentino et al. (2020) for three spectroscopically confirmed $z \sim 4$ quiescent galaxies, two of which have poststarburst-like SEDs. This is critical to this work since poststarburst galaxies, with young stellar ages and therefore bluer colors, are often excluded in quiescent galaxy studies at $z > 3$ as the majority do not fall into the *UVJ* quiescent region at high z (Merlin et al. 2018; Carnall et al. 2020; Stevans et al. 2021; Lovell et al. 2023). All three SEDs were modeled with >10 photometric measurements covering $\lambda_{\rm rest} = 0.4$–10 μm, ensuring a well-constrained rest-frame UV-to-near-infrared SED that traces the shape and strength of the Balmer 4000 Å break, as well as any UV emission from young stellar populations. We redshift these SEDs from $z = 3$–6 to chart their evolution through our proposed color space.

We also include 124 "robust" quiescent galaxy candidates at $3 < z < 5$ identified in Gould et al. (2023). These candidates were selected first based on their SED-derived photo-z values and stellar masses using photometry from the COSMOS2020 catalog (Weaver et al. 2022), which then were further required to have a >95% probability of belonging to a quiescent "group" as defined by a Gaussian mixture model trained on $2 < z < 3$ galaxies. The model was trained over several combinations of rest-frame near-ultraviolet (NUV), *U*, *V*, and *J* colors and is more complete in selecting poststarburst galaxies and has less contamination from dusty interlopers when compared to the classic *UVJ* method from Williams et al. (2009).

Finally, we also generate mock quiescent galaxy SED models generated via the BEAGLE tool (Chevallard & Charlot 2016) using the Bruzual & Charlot (2003) templates; these mock SEDs are at solar metallicity, with one model representing an older (1 Gyr) stellar population and the other representing a younger (500 Gyr) stellar population, both generated using a delayed-τ star formation history (SFH) where $\tau = 100$ and 60 Myr, respectively. We also apply varying levels of attenuation ($A_V = 0$–2) to examine the effects of dust on quiescent galaxy colors.

2.2. *Dusty Star-forming Galaxies*

To model the NIRCam colors of DSFGs (see Casey et al. 2014), we use the SEDs of ALESS submillimeter galaxies[32] from da Cunha et al. (2015). Specifically, we use ALESS SEDs averaged according to varying levels of *V*-band dust attenuation (A_V) to visualize how DSFG NIRCam colors change as a function of attenuation. This is important because the dust-reddened stellar continuum of DSFGs can mimic the red colors of ancient stellar populations in quiescent galaxies and contaminate the quiescent region of *UVJ* diagrams (Martis et al. 2019). ALESS SEDs were modeled using a rich set of ultraviolet to radio photometry and have a median redshift of $z = 2.7 \pm 0.1$. We use the SED templates corresponding to $A_V < 1$ (blue, little attenuation), $A_V \geqslant 3$ (red, significant attenuation), and the overall average SED with $A_V \sim 2$. We redshift these SED templates from $z = 1$ to 6 to model their color evolution (shown in purple in Figure 1).

3. Quiescent Galaxy Selection at $z > 3$

Our ultimate goal is to select both aged and young quiescent galaxies at $z > 3$ from an informed, contextualized, and manageable parent sample. By using the observed-frame colors of empirically constrained SEDs described in the previous section, we are able to understand that the majority of objects in this color space are likely high-z quiescent galaxies, $z < 3$ DSFGs, and/or emission line galaxies in a discrete redshift range (also further described in Section 4.4). This knowledge provides distinct constraints on the SED modeling space that can and will be probed for sources in this color space, and also provides a clear path forward for follow-up observations on ruling out contaminants. In the following paragraphs, we describe the details of how we defined this color space, and then in the section after, we combine this with SED fitting to identify candidate $z \gtrsim 3$ quiescent galaxies.

In the canonical rest-frame *UVJ* diagram, the $U - V$ plane spans the Balmer/D$_n$ (4000 Å) break prominent in galaxies whose light is dominated by aged stellar populations, while the $V - J$ component involves a near-infrared detection to break degeneracies between quiescent galaxies and galaxies with spectra reddened by heavy dust obscuration (i.e., DSFGs). However, at $z > 3$, the rest-frame *J*-band is redshifted out of NIRCam's spectral window for galaxies at these epochs, and into wavelengths observable by MIRI. Unfortunately, MIRI, with its smaller field of view, will not fully cover the NIRCam imaging for many of the early JWST legacy surveys currently

---

[32] http://astronomy.swinburne.edu.au/~ecunha/ecunha/SED_Templates.html

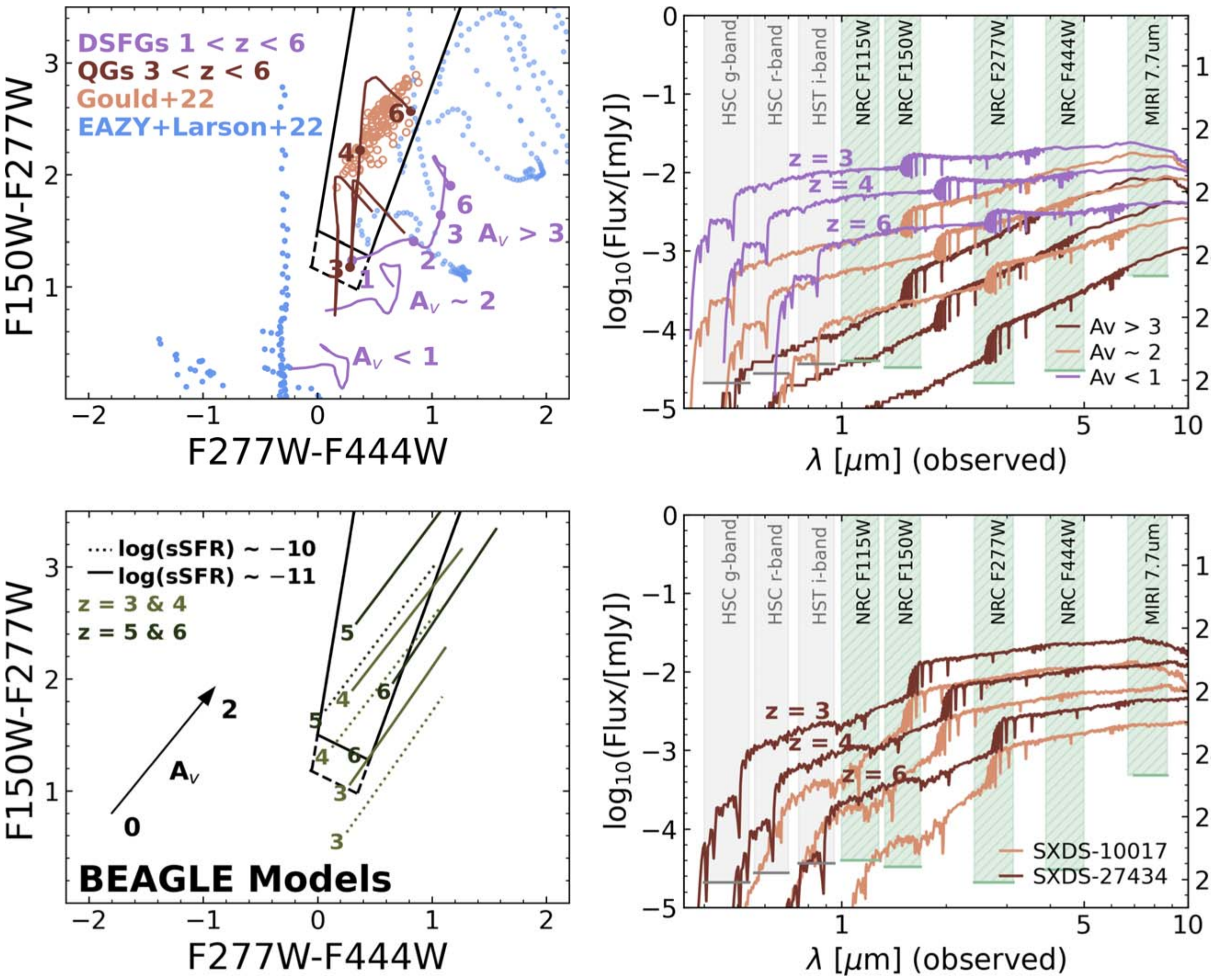

Figure 1. Left: F277W − F444W vs. F150W − F277W colors for empirically constrained galaxy SED templates (top) and mock young and old quiescent galaxy SEDs generated by BEAGLE (bottom), described in Section 2. The black line marks the "short" wedge boundaries, while the dashed line marks the "long" wedge extension. The former is less complete but also has fewer contaminants, while the latter captures most quiescent galaxies at $3 < z < 6$ but with higher rates of contamination. In the top panel, we show dusty, star-forming galaxy (DSFG) SEDs redshifted from $z = 1$ to 6 in purple (da Cunha et al. 2015, also shown in the top right panel), quiescent galaxies at $z \sim 4$ redshifted from $z = 3$ to 6 in red (Valentino et al. 2020, also shown in the bottom right panel), and emission line galaxy SEDs redshifted from $z = 3$ to 20 in blue (Larson et al. 2023). Right: the top panel shows observed-frame galaxy SEDs redshifted to $z = 3$, 4, and 6. As an example JWST survey that is ideal for this search, we overlay the 5σ photometric limits of various wide-band surveys that cover the COSMOS-Web field (Casey et al. 2023). Purple, orange, and brown lines are the redshifted SEDs of $z \sim 2$–3 ALESS submillimeter galaxies from da Cunha et al. (2015), progressing from low V-band attenuation ($A_v < 1$), to average ($A_v \sim 2$), to highly attenuated ($A_v \geqslant 3$), respectively. The bottom panel shows the SEDs of spectroscopically confirmed $z \sim 4$ quiescent galaxies from Valentino et al. (2020), redshifted to $z = 3$, 4, and 6. The brown SED corresponds to SXDS-10017, a more evolved quiescent galaxy at $z_{\rm spec} = 3.767$, and the orange SED corresponds to SXDS-27434, a poststarburst galaxy at $z_{\rm spec} = 4.013$. The third quiescent galaxy (COS-466654) is not shown for simplicity, though is included in the SED tracks in the top left color space.

underway (e.g., only the MIRI F770W filter will image ∼35% of the widest Cycle 1 JWST survey, COSMOS-Web; Casey et al. 2023). This is critical because quiescent galaxies at $z > 3$ are exceedingly rare according to pre-JWST number density estimates ($n \sim 10^{-5}$–10^{-6} Mpc^{-3}; Toft et al. 2014; Valentino et al. 2020; Nanayakkara et al. 2024). Wide-field surveys with deep, multiband coverage are critical to detecting statistically significant samples of these objects and/or confirming the newer (higher) JWST-derived number density estimates that were calculated over smaller area surveys ($n \sim 10^{-4}$–10^{-5} Mpc^{-3}; Carnall et al. 2023; Valentino et al. 2023). Thus, to optimize efficiency and applicability across wide-field surveys, we design this selection technique to use NIRCam filters that are available among the majority of recent and upcoming JWST surveys including COSMOS-Web (Casey et al. 2023), CEERS (Finkelstein et al. 2017; Bagley et al. 2023), JADES (Bunker et al. 2020), PANORAMIC (Williams et al. 2021), and PRIMER (Dunlop et al. 2021).

Our first goal is to isolate the Balmer/D$_n$ (4000 Å) break at $3 < z < 5$. At these epochs, the Balmer/D$_n$ (4000 Å) break redshifts to $\lambda_{\rm observed} = 1.6$–2.4 μm. We wish to define a set of filters that brackets the Balmer break, instead of directly detects it. In other words, the NIRCam F200W band, with a filter throughput that spans $\lambda = 1.7$–2.2 μm, will not directly measure the Balmer break but instead exhibit significant variance depending on the redshift of the quiescent galaxy. The F200W band is therefore not a reliable tracer at $3 < z < 5$. Instead, for all quiescent galaxies at $3 < z < 5$, the Balmer break sits nicely between the F150W and F277W filters (Figure 1). This is also advantageous because the majority of major Cycle 1 JWST surveys have F150W and F277W imaging.

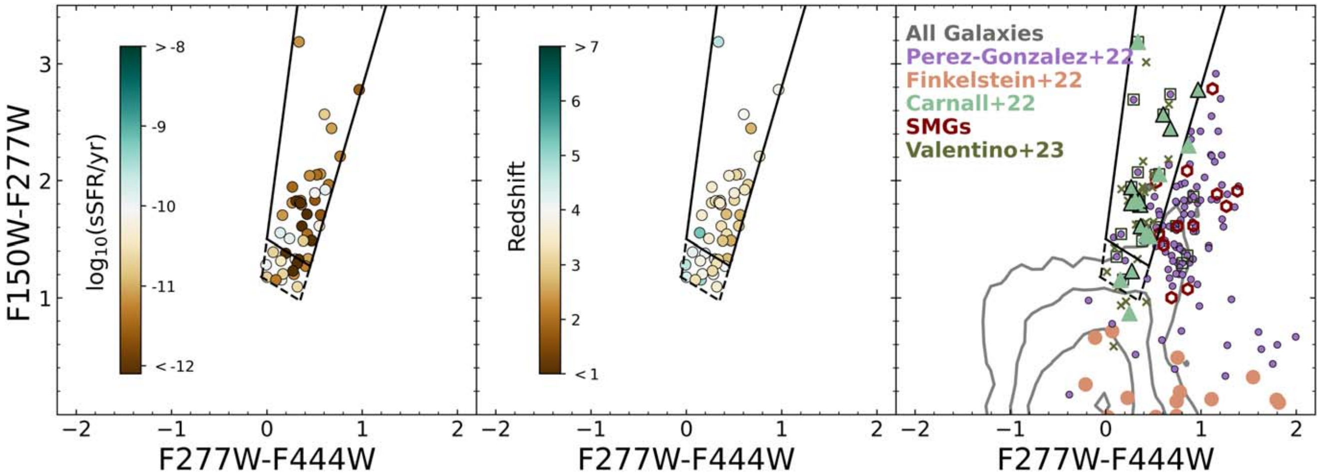

Figure 2. F277W − F444W vs. F150W − F277W colors for $2.5 < z < 5$ quiescent galaxy candidates detected in CEERS using the proposed color selection method (including $z_{\rm phot} \geqslant 2.5$ and $\log_{10}({\rm sSFR/yr}) \lesssim -10$). Interlopers in this color space are further described in Section 4.4 and shown in the Appendix, Figure A2. Left: the final sample of 44 candidate galaxies colored by their specific star formation rate (sSFR). Middle: the same sample colored by photometric redshift. Right: all CEERS objects in the F277W − F444W vs. F150W − F277W color space and SNR ⩾ 3 in all three NIRCam bands (gray contours). Green triangles mark quiescent galaxy candidates from Carnall et al. (2023), where the most "robust" candidates (as defined therein by their sSFR posteriors) are outlined in black. Purple points mark red objects identified by Pérez-González et al. (2023), with the quiescent galaxy candidates (also defined by sSFR limits) outlined in black squares. Galaxies with SCUBA-2 and NOEMA detections (i.e., dust obscured) are outlined in red (Zavala et al. 2023). For reference, we also include the ultrahigh-z sample of objects characterized in Finkelstein et al. (2023) in pink.

To distinguish between dust-reddened star-forming galaxies and quiescent galaxies, we introduce a third NIRCam band: F444W. As shown in Figure 1, increasing dust attenuation results in redder F277W − F444W colors, whereas dust-free star-forming galaxies and quiescent galaxies have relatively flat spectral slopes between these two bands.

In total, we use three NIRCam bands to define this color space: F150W, F277W, and F444W. Using the SED templates described in the previous section, we tested a variety of "wedges" in this color space and identified several regions of critical thresholds that have varying degrees of completeness and contamination. In this paper, we share the two versions with the least amount of contamination, while the most complete (but highly contaminated) wedge is listed in the Appendix. In all cases, we require that objects be detected with a signal-to-noise ratio (SNR) threshold ⩾3 in all three NIRCam bands. In order to be considered a quiescent galaxy candidate at $3 < z < 6$, the most conservative color threshold (aka the "short wedge") requires that objects have NIRCam colors that meet the following criteria (all in the AB magnitude system):

$$\begin{aligned}&\text{A. } ({\rm F150W} - {\rm F277W}) < 1.5 + 6.25 \\ &\quad \times ({\rm F277W} - {\rm F444W}) \\ &\quad \text{and} \\ &\text{B. } ({\rm F150W} - {\rm F277W}) > 1.5 - 0.5 \times ({\rm F277W} - {\rm F444W}) \\ &\quad \text{and} \\ &\text{C. } ({\rm F150W} - {\rm F277W}) > 2.8 \times ({\rm F277W} - {\rm F444W}).\end{aligned} \tag{1}$$

The short wedge is represented by solid black lines in Figures 1 and 2. The short wedge has the most minimal contamination by dust-obscured galaxy SED templates but, depending on the BEAGLE models or the empirically constrained SEDs, this wedge likely misses poststarburst quiescent galaxy SEDs at $z < 4$ as their slightly bluer colors push them south of the short wedge's bounds.

To better capture poststarburst galaxies at $z < 4$, we introduce a wedge that pushes slightly bluer in both color spaces. This "long wedge" requires that Criterion B of the short wedge is changed to:

$$({\rm F150W} - {\rm F277W}) > 1.15 - 0.5 \times ({\rm F277W} - {\rm F444W}). \tag{2}$$

The long wedge is represented by the additional region of black dashed lines in Figures 1 and 2. According to the SED templates and BEAGLE models, the long wedge is potentially more complete in the $z > 3$ quiescent galaxy population, but also likely has higher contamination by dusty galaxies and star-forming galaxies.

It is important to note that, based on the SEDs and BEAGLE models in Figure 1, if there exists substantial populations of dusty quiescent and/or poststarburst galaxies at $z > 3$, the proposed color space may only capture a subset of them. These sources—which thus far have only been speculative due to tentative photometrically derived constraints—would represent a potential "missing link" between $z > 3$ DSFG and quiescent galaxy populations (e.g., Rodighiero et al. 2023), and are therefore a potentially interesting and important population. These sources would be more likely captured in our proposed "red selection wedge" shared in the Appendix, though future observations are needed to confirm their existence.

4. Applied to CEERS

4.1. CEERS Data

In Figure 2, we show our color selection method applied to CEERS NIRCam catalogs, including all ten 2022 June and December pointings. The imaging data and reduction are described in detail in Bagley et al. (2023). The photometry is performed in two image mode using SOURCE EXTRACTOR (Bertin & Arnouts 1996) on a (weighted sum) combined F277W and F356W image. Details of the photometry extraction procedure are similar to the method presented in Finkelstein et al. (2023), with a few updates. Specifically, Hubble Space Telescope (HST)/Advanced Camera for Surveys (ACS) F606W and F814W mosaics from CANDELS

(Koekemoer et al. 2011; Grogin et al. 2011; Faber 2011), as well as JWST/NIRCam F115W, F150W, and F200W data were convolved to match the point-spread function (PSF) of NIRCam F277W imaging. For images with larger PSFs than the F277W imaging (HST/WFC3 F105W, F125W, F140W, and F160W data from CANDELS, as well as NIRCam F356W, F410M, and F444W), we derive a correction factor by convolving the F277W image to the larger PSF, then measuring the flux ratio in the original versus convolved image. This correction factor is applied to fluxes measured in the images with larger PSFs to account for any missing flux in the aperture defined by the F277W image (under the assumption that the morphology does not change significantly).

Object fluxes were corrected twice more to capture any potential flux missed on larger scales: once by the ratio between the flux measured in small Kron apertures to the default larger `MAG_AUTO` Kron aperture, and then an additional ∼5%–20% correction to account for missing flux from the wings of the PSF (as determined by source injection simulations).

The final photometric catalog used in this paper includes the full CEERS suite of imaging data: NIRCam F115W, F150W, F200W, F277W, F356W, F410M, and F444W filters, as well as existing CANDELS HST/ACS and WFC3 data in the F606W, F814W, F105W, F125W, F140W, and F160W bands. Photometric redshifts were also calculated for the entire catalog using the method presented in Finkelstein et al. (2023).

After filtering for sources with SNR $\geqslant 3$ in the F150W, F277W, and F444W bands, we are left with ∼50,000 objects in the CEERS pointings covering ∼97 arcmin^2. In the short wedge we retrieve a total of 82 objects, while in the long wedge we retrieve 236 objects (82 of which are the same objects in the short wedge). These selected objects represent ≈0.2% and 0.5% of the SNR $\geqslant 3$ catalog, respectively, further highlighting the significant reduction in sample size and increase in efficiency when filtering and analyzing large catalogs for high-z quiescent galaxies.

4.2. Spectral Energy Distribution Fitting

For all sources within our defined wedge, we use the CIGALE (Burgarella et al. 2005; Noll et al. 2009; Boquien et al. 2019) to generate galaxy SEDs and photometric redshifts. We assume a Chabrier (2003) IMF, Bruzual & Charlot (2003) stellar population synthesis models, and the Calzetti et al. (2000) dust attenuation law. The V-band attenuation was allowed to vary between 0 and 5 mag, and gas and stellar metallicities were fixed to solar ($Z_\odot = 0.02$). We include the option for nebular emission with an ionization parameter between $\log_{10} U = [-2, -3]$, and allow the redshift to vary uniformly between 0.8 and 20 in steps of $\delta z = 0.1$. We assume a delayed SFH (delayed-τ). For the main stellar population, we fit over a wide range of e-folding times (10–5000 Myr). We also allow an optional late burst of star formation, with an e-folding time varying between 10 and 300 Myr and a potential fraction of stellar mass created by the late burst to vary between 0% and 50%.

4.3. Quiescent Galaxies in CEERS

4.3.1. Selection and Characteristics

When using only photometry to identify high-z quiescent galaxies, issues with sample completeness and contamination are perhaps mitigated best by defining thresholds in galaxy sSFR (=SFR/$M_\star$). The majority of star-forming galaxies lie on a well-established SFR–$M_\star$ relationship (e.g., Noeske et al. 2007; Speagle et al. 2014), with quiescent galaxies falling 1–2 dex below this plane (e.g., Straatman et al. 2014; Pacifici et al. 2016). Working with an sSFR threshold is likely more advantageous at $z > 3$ as this method provides more flexibility in capturing galaxies that are either in the process of quenching ("green valley" objects), or recently quenched objects with leftover UV emission from the last generation of young stars ("poststarbursts").

We select high-z quiescent galaxy candidates as objects with $z_{\rm phot} \geqslant 2.5$ and $\log_{10}({\rm sSFR/yr}) \lesssim -10$, and present these candidates in Table 1. In the short wedge, this yields a total of 30 candidates, while the long wedge adds another 15 candidates, making a total of 45 high-z quiescent galaxy candidates. As mentioned later in Section 4.4, we remove a single source that is coincident within 1″ of a submillimeter source and is therefore likely a heavily obscured interloper. The remaining 44 sources span $z = 2.6$–5.3 with a median redshift of $z \sim 3.5$. They are relatively massive with a median stellar mass of $M_\star \approx 3 \times 10^{10}\ M_\odot$, and quiescent with a median $\log_{10}({\rm sSFR/yr}) \approx -11.2$. We also note that all but one of our candidates have $\geqslant 3\sigma$ detections at $m_{\rm F150W} < 28$, while the CEERS survey reaches 5σ depths of $m_{\rm F150W} \sim 29$ (Bagley et al. 2023); therefore, this color selection method can be safely and successfully applied to shallower JWST surveys (e.g., COSMOS-Web with 5σ depths up to $m_{\rm F150W} \approx 28$; Casey et al. 2023).

As shown in Figure 2, nearly all (14/15) of the CEERS quiescent galaxy candidates presented in Carnall et al. (2023) are recovered in our analysis (both by nature of their loci on the color diagram, but then again by our SED-fitting procedure). Out of the 25 quiescent galaxy candidates in Pérez-González et al. (2023), 22 meet the SNR thresholds, and only 18/22 fall in the long wedge. Our SED results recover 11 of the 18 candidates as quiescent galaxies $z \geqslant 2.5$. We find that three galaxies designated as star-forming in Pérez-González et al. (2023) are also recovered as quiescent in this work, though our analysis prefers lower redshift solutions for two of these objects ($\delta z \sim 1$) than those presented in Pérez-González et al. (2023), which is likely driving the discrepant star-forming properties. The remaining quiescent candidates in Pérez-González et al. (2023) are fit as coeval star-forming (or even bursting) galaxies in our SED-fitting process with $\log_{10}({\rm sSFR/yr}) \sim -9$ to -8 and $A_V \sim 2$–4. For the majority of objects that overlap as quiescent galaxy candidates in Carnall et al. (2023) and/or Pérez-González et al. (2023), our analysis produces photometric redshifts within $\Delta z \approx 0.5$.

We also compare against the 24 CEERS quiescent galaxy candidates from (Valentino et al. 2023) and find that 19 of these candidates fall into the long wedge space. The five sources that fall outside the wedge have lower stellar masses than those within the wedge (with $< \log_{10} M_\star > = 9.45\ M_\odot$ and $10.74\ M_\odot$, respectively) and were reported to show features signifying more recent quenching. Of the objects that fall into the wedge, we recover 14 quiescent galaxy candidates at $z \gtrsim 3$. The remaining five objects are fit as coeval starburst-like galaxies with $\log_{10}({\rm sSFR/yr}) = -9$ to -8 and $A_V \sim 2$–3, further highlighting the difficulty in dividing these two galaxy populations with photometry alone.

Perhaps more notable than the recovery of previously identified high-z quiescent galaxy candidates is the discovery

Table 1
Final Sample of 44 Quiescent Galaxy Candidates at $2.5 < z < 6$ in CEERS

R.A.	Decl.	m_{150W}	Redshift	$\log_{10}(M_\star/M_\odot)$	$\log_{10}(\mathrm{sSFR/yr})$	Other References[a]	Other Selection Methods[b]
215.01238622	53.01419481	27.50 ± 0.18	4.20 ± 0.19	9.19 ± 0.03	−10.6	V	AD
214.85898311	52.89504924	25.54 ± 0.04	4.20 ± 0.03	10.0 ± 0.02	−12.0	⋯	AD
214.93142047	52.93742617	25.91 ± 0.06	4.91 ± 0.24	9.77 ± 0.03	−10.1	C	⋯
214.91938331	52.92730122	27.03 ± 0.08	4.68 ± 0.18	9.31 ± 0.02	−9.98	⋯	⋯
214.75157628	52.82993207	25.24 ± 0.02	4.00 ± 0.02	10.2 ± 0.02	−11.2	⋯	⋯
214.82580314	52.88008725	24.19 ± 0.02	3.59 ± 0.01	10.2 ± 0.05	−10.6	⋯	⋯
214.82613200	52.88003104	28.43 ± 0.16	3.78 ± 0.37	8.79 ± 0.04	−10.4	⋯	AD, UVJ^{B}
214.85799854	52.87626021	25.55 ± 0.12	3.87 ± 0.13	9.84 ± 0.02	−10.6	⋯	AD
214.85621998	52.86111432	25.62 ± 0.04	3.61 ± 0.04	9.88 ± 0.02	−10.1	⋯	⋯
214.70744282	52.75260243	24.25 ± 0.02	3.10 ± 0.02	10.4 ± 0.02	−12.0	⋯	AD
214.78830547	52.80054129	25.42 ± 0.03	3.89 ± 0.02	9.89 ± 0.02	−11.1	⋯	⋯
214.75193946	52.74879797	26.43 ± 0.05	4.32 ± 0.11	9.43 ± 0.02	−10.7	⋯	⋯
214.90955075	52.87502532	25.18 ± 0.02	3.30 ± 0.02	9.99 ± 0.02	−12.0	⋯	AD
214.89561652	52.85649304	22.93 ± 0.01	3.19 ± 0.02	10.8 ± 0.02	−12.0	C, V	AD
215.10403091	52.96502357	27.40 ± 0.13	3.29 ± 0.18	8.91 ± 0.04	−11.3	⋯	AD
214.95787657	52.98030101	25.13 ± 0.02	3.53 ± 0.15	10.4 ± 0.04	−11.4	PG, C	AD, G, UVJ^{V}
214.98181750	52.99123408	24.29 ± 0.01	3.38 ± 0.10	10.7 ± 0.03	−11.1	PG, C, V	AD, G, $UVJ^{V,B}$
215.03905173	53.00277846	26.49 ± 0.07	4.00 ± 0.56	10.5 ± 0.07	−10.7	PG, C, V	AD, G, $UVJ^{V,B,W}$
214.90484984	52.93535040	24.69 ± 0.02	3.28 ± 0.09	10.4 ± 0.03	−12.7	PG, C, V	AD
214.86604381	52.88408282	24.86 ± 0.02	3.73 ± 0.18	10.7 ± 0.04	−11.1	PG, C, V	AD, G, $UVJ^{V,B,W}$
214.87871537	52.88783356	26.87 ± 0.15	3.60 ± 0.23	9.43 ± 0.06	−9.92	V	AD, UVJ^{B}
214.87909817	52.88805928	25.40 ± 0.03	3.40 ± 0.10	10.2 ± 0.04	−12.0	PG, C, V	AD
214.76062446	52.84531499	23.11 ± 0.01	3.30 ± 0.14	11.2 ± 0.03	−11.1	C, V	AD, G, UVJ^{V}
214.83685708	52.87344970	24.61 ± 0.02	3.28 ± 0.10	10.4 ± 0.04	−11.4	PG, C, V	AD
214.76722738	52.81771171	24.94 ± 0.03	3.53 ± 0.18	10.5 ± 0.04	−11.4	PG, V	AD, G, UVJ^{V}
214.85057925	52.86601995	25.68 ± 0.04	2.69 ± 1.07	10.6 ± 0.19	−11.0	PG, C	G, UVJ^{V}
214.80816482	52.83221612	27.82 ± 0.13	4.71 ± 0.22	10.2 ± 0.04	−11.1	PG, C, V	AD, G, $UVJ^{V,B,W}$
214.76280726	52.85128125	26.61 ± 0.07	3.12 ± 0.36	10.0 ± 0.05	−11.4	PG	AD, G, $UVJ^{V,B,W}$
214.85390175	52.86135518	25.26 ± 0.04	3.86 ± 0.29	11.3 ± 0.06	−11.5	PG, C	AD
214.79996984	52.82209160	25.83 ± 0.03	2.70 ± 0.30	10.1 ± 0.06	−11.6	PG	AD, G, $UVJ^{V,B,W}$
214.75817573	52.78721770	25.64 ± 0.04	2.99 ± 0.13	10.2 ± 0.06	−10.2	⋯	AD, G, UVJ^{V}
214.97856151	52.92153875	24.89 ± 0.03	2.61 ± 0.14	10.4 ± 0.03	−12.0	⋯	AD, G, $UVJ^{V,B,W}$
214.94173278	52.88455850	26.15 ± 0.05	3.06 ± 0.39	10.3 ± 0.06	−11.3	⋯	AD, G, $UVJ^{V,B,W}$
214.82773594	52.82376795	24.22 ± 0.02	2.85 ± 0.19	10.5 ± 0.05	−10.7	PG, V	AD, G, UVJ^{V}
215.06584489	52.93295198	24.45 ± 0.03	3.48 ± 0.14	10.6 ± 0.05	−12.1	⋯	AD
215.11517784	52.96071251	24.03 ± 0.02	2.75 ± 0.15	10.6 ± 0.03	−11.0	⋯	AD, G, $UVJ^{V,B,W}$
215.02644074	52.89377290	24.90 ± 0.03	2.77 ± 0.16	10.5 ± 0.04	−12.6	⋯	AD, G, $UVJ^{V,B,W}$
215.04445349	52.89882060	27.74 ± 0.24	5.27 ± 0.28	9.38 ± 0.08	−9.84	⋯	AD, UVJ^{B}
214.98925860	52.84716447	25.22 ± 0.02	3.19 ± 0.17	10.4 ± 0.04	−11.6	⋯	AD, G, UVJ^{V}
214.89491218	52.81715613	25.82 ± 0.04	3.53 ± 0.47	10.6 ± 0.05	−11.2	⋯	AD, G, UVJ^{V}
214.93252224	52.83243848	26.61 ± 0.17	3.52 ± 0.34	9.58 ± 0.06	−11.1	⋯	AD
214.97116080	52.85489138	25.53 ± 0.03	3.66 ± 0.14	10.4 ± 0.04	−11.1	⋯	AD, G, $UVJ^{V,B}$
214.89703386	52.79221821	25.34 ± 0.03	3.35 ± 0.33	10.4 ± 0.08	−9.93	⋯	AD
214.77381122	52.74001063	25.11 ± 0.05	3.62 ± 0.51	10.5 ± 0.09	−10.0	⋯	AD

Notes.

[a] PG corresponds to sources captured in Pérez-González et al. (2023), C corresponds to sources listed in Carnall et al. (2023), and V corresponds to sources listed in Valentino et al. (2023).

[b] AD corresponds to sources captured by the $(ugi)_s$ color selection technique presented in Antwi-Danso et al. (2023), and G is for sources captured by the combination color and probabilistic selection technique from Gould et al. (2023). *UVJ* is for sources captured by a specific *UVJ* selection wedge, where V corresponds to the padded wedge presented in Valentino et al. (2023), B is for the modified wedge presented in Belli et al. (2019), and W is for the original wedge presented in Williams et al. (2009).

of many new ones. When we reduce our candidate pool to objects discovered in the same CEERS pointings as those presented in Pérez-González et al. (2023), Carnall et al. (2023), and Valentino et al. (2023)—specifically pointings 1, 2, 3, and 6—we identify an additional 13–14 new $z > 3$ quiescent galaxy candidates. This is a near doubling of the candidate population in these pointings, however the majority of these new candidates are clustered in two pointings, yielding source densities 2–4× higher than in the other pointings. This may be evidence of a nascent galaxy protocluster—which is possible at these epochs (Tanaka et al. 2023). Indeed, there is spectroscopic evidence of such a structure in the CEERS field (Jin et al. 2024), but only one of our sources is a known member thus far and additional follow-up spectroscopic observations are required to confirm whether the remaining new objects belong to such a structure.

The average sSFR for the newly discovered population is $\log_{10}(\mathrm{sSFR/yr}) = -10.4 \pm 0.4$, but for the previously discovered population it is $\log_{10}(\mathrm{sSFR/yr}) = -11.1 \pm 0.4$. These population characteristics suggest that this color selection

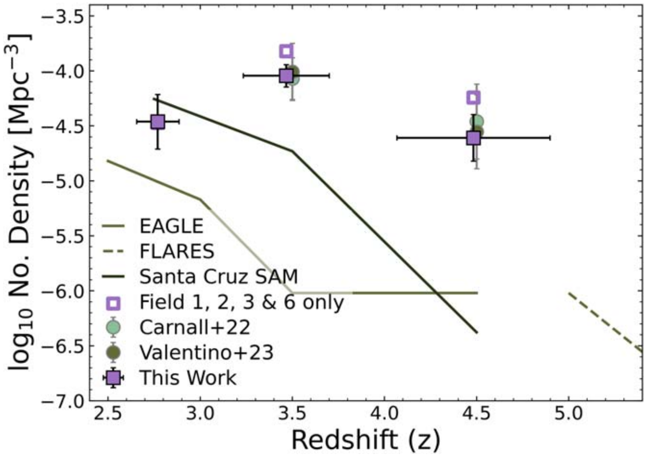

Figure 3. Number density evolution derived using the sample of quiescent galaxies identified in this work (purple squares, also listed in Table 2). The other two sets of points are the reported number densities of quiescent galaxies derived also using JWST data (Carnall et al. 2023; Valentino et al. 2023); the discrepancy between our estimates and Valentino et al. (2023) is likely due to differences in stellar mass thresholds (discussed further in Section 4.3). We also overlay predictions from several cosmological simulations described in Section 5 and shown in Figure 5.

technique is successful in capturing young, poststarburst quiescent galaxies as well as more evolved galaxies with little to no young stellar populations. Such a population yield is critical as most quiescent galaxies at these epochs are expected to be poststarbursts (with $\log_{10}(\mathrm{sSFR/yr}) = -10$ to -11; D'Eugenio et al. 2020a). However, when using the age–color trend defined in Belli et al. (2019) and explored in Park et al. (2023; see Figure 4), we find that only ∼20% ($N = 9$) of our sample qualifies as "rapidly quenched" with colors indicative of median stellar ages < 300 Myr (the upper limit of 800 Myr in Belli et al. 2019 only increases the sample to $N = 10$). These sources are not statistically distinct from the larger sample in terms of sSFR, stellar mass, or redshift. This may indicate that a large fraction of our sample may have already passively evolved for several hundred megayears prior to observation, and/or may not have had such an extreme degree of starburstiness or rapid quenching as the $z_{\mathrm{spec}} \sim 1$–2 samples examined in the aforementioned studies.

More details on the properties of the quiescent galaxy candidate sample in this work and across other public JWST Cycle 1 surveys will be presented in a forthcoming paper (A. S. Long et al. 2024, in preparation).

4.3.2. Number Densities

In Figure 3, we derive number densities across redshift ranges of $z = [2.5, 3)$, [3, 4), and [4, 5). To derive conservative uncertainties on these estimates, we ran 10^3 Monte Carlo simulations that sampled each object's redshift from a uniform prior defined by their photo-z estimate plus/minus their respective 1σ uncertainties. We calculate the number density in each redshift bin for each realization, and then report the median number densities for this work. Uncertainties were derived from the inner 68% confidence interval of the Markov Chain Monte Carlo–computed values plus Poisson noise. These estimates are presented in Table 2.

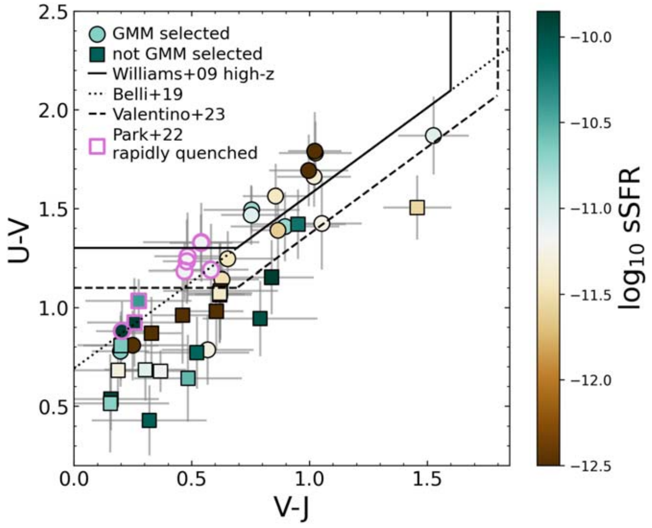

Figure 4. Rest-frame *UVJ* color–color diagram of the 44 candidate quiescent galaxies at $z > 3$. Marker colors correspond to sSFRs. Circles represent the sources selected via the Gaussian mixture model presented in Gould et al. (2023), while squares represent sources that are not. Pink outlines mark the young, rapidly quenched sources according to Belli et al. (2019) and Park et al. (2023). The solid black line marks the $z > 1$ quiescent region from Williams et al. (2009); the dashed marks the "padded" region from Valentino et al. (2023); and the dotted line marks the poststarburst extension from Belli et al. (2019).

Table 2
Number Density of Quiescent Galaxies Identified in this Work

Redshift Range	Number	n/Mpc^{-3}
$2.5 < z < 3$	7	$3.45^{+2.66}_{-1.50} \times 10^{-5}$
$3 < z < 4$	29	$9.04^{+2.42}_{-1.91} \times 10^{-5}$
$4 < z < 5$	8	$2.45^{+1.62}_{-0.98} \times 10^{-5}$

We compare our number density estimates to other literature studies that uses JWST data in their selection of massive quiescent galaxies, namely, Carnall et al. (2023) and Valentino et al. (2023). When calculated over the entire CEERS field, our estimates are in excellent agreement with those derived in Carnall et al. (2023) and Valentino et al. (2023; specifically the CEERS-only result therein), despite different selection techniques over similar fields/data sets. However, when calculated over the same four pointings in Carnall et al. (2023) and Valentino et al. (2023; i.e., Fields 1, 2, 3, and 6), we find our number density estimates at $z > 3$ are roughly 1.5–2× (∼0.2–0.3 dex) higher, though within the 1σ uncertainties. This is due to the additional discovered sources that may belong to a potential $z \sim 3$–4 overdensity of quiescent galaxies in the CEERS field (see, e.g., Jin et al. 2024). Therefore, the population densities derived via our proposed color selection technique (the long wedge, specifically), when combined with SED fitting, appear generally consistent with other high-z quiescent galaxy selection techniques. In a forthcoming paper, we will explore how these number densities vary as a function of sSFR, stellar mass, and more with a larger sample of quiescent galaxy candidates selected using this method.

4.3.3. Are They Captured with Other Selection Techniques?

In addition to an sSFR threshold, the majority of quiescent galaxy selection techniques use rest-frame color–color diagrams to distinguish these sources from star-forming galaxies. We applied these techniques to our sample and find that none capture all of our candidate sources (see Table 1 and Figure 4).

The classic $z > 1$ *UVJ* diagram, first shown in Williams et al. (2009), has the lowest successful selection rate, with only ∼30% ($N = 14$) of our candidates being classified as quiescent. Modified versions of the *UVJ* diagram, including those modified to better detect young, poststarburst-like sources (e.g., Belli et al. 2019) or loosened to allow for more color uncertainty (Valentino et al. 2023), perform slightly better by capturing roughly 35%–45% of our candidates ($N = 15$ and 20, respectively). As seen in Valentino et al. (2023), the novel method presented in Gould et al. (2023), which utilizes an additional NUV color and assigns a quiescent probability based on Gaussian mixture models in the NUV – U versus $V - J$ color space, performs similarly to the padded *UVJ* diagram in Valentino et al. (2023). Finally, we applied the synthetic $(ugi)_s$ method presented in Antwi-Danso et al. (2023) and find the highest rate of selection at ∼85% ($N = 37$).

Only seven objects in total are not selected by at least one of these other techniques, which may indicate that our proposed method may be more successful in identifying $z \gtrsim 3$ quiescent galaxy candidates. However, it is entirely possible that these objects (and several others) are moderately dusty sources that are not sufficiently IR luminous to be captured by existing IR/submillimeter surveys (see next section for more details). Thus, until follow-up observations can confirm the nature of our candidate sources, we will not know the true contamination rate of this sample, which means that one or more of these other color selection techniques may in all actuality have complete overlap with ours. Future investigations with perhaps larger samples and more multiwavelength coverage will be critical for assessing the efficacy of this and the aforementioned selection techniques.

4.4. Contaminants

In the long (short) wedge, there are 191 (52) objects that do not meet the criteria for quiescent galaxy candidates at $z > 2.5$. We describe in this section some of the properties of these contaminant galaxies, and show in the Appendix some of their SED-derived properties. At a high level, there is unfortunately no clear threshold in flux/magnitude across the HST and JWST bands that easily separates the contaminants from the high-z quiescent galaxy candidates. Future spectroscopically confirmed samples will certainly help identify any potential additional thresholds that could be applied to further reduce the contaminant population.

The majority (≳80%) of the contaminant objects are fit as emission line/starburst-like galaxies at $z \lesssim 6$. Redshifted nebular emission lines (such as Hα and Hβ) can contribute significant flux to wide bandpasses, thereby making a galaxy appear redder than it truly is (Labbé et al. 2013; Smit et al. 2016; Schreiber et al. 2018; Antwi-Danso et al. 2023; McKinney et al. 2023). For visual demonstration of contamination in the color space, we redshift SED templates of galaxies with strong emission lines from $z = 1$ to 20 using the latest set of templates from the photo-z fitting code EAZY (Brammer et al. 2008; derived from the Flexible Stellar Population Synthesis code in Conroy & Gunn 2010). We include an additional set of SED templates (Larson et al. 2023, set 3.5)[33] developed to model strong emission line emitters and ultrablue galaxies at high z. We show these interpolated colors in Figure 1. We find that emission line galaxies enter the long wedge color space at $z \sim 4$–5 and $z \sim 14$. The latter ultrahigh redshift population can be removed using a magnitude threshold in the F115W band: nearly all (25/26) of the $z > 8$ candidate galaxies presented in Finkelstein et al. (2023) have $\mathrm{m_{F115W}} < 28$ (AB mag), while all but one of our candidate quiescent galaxies have $\mathrm{m_{F115W}} > 28$ (AB mag).

We performed a similar analysis to assess for potential contamination from active galactic nuclei (AGN). We evolved AGN SED templates using SEDs from the SWIRE Template Library[34] from $z = 1$ to 10. For Type 1 (unobscured) AGN, we used the QSO1 template that combines rest-frame optical to mid-infrared spectra for a sample of spectroscopically confirmed quasars (Hatziminaoglou et al. 2005). For Type 2 (obscured) AGN, we use the IRAS19254-7245 South SED which is a template with a combined starburst and Seyfert 2 AGN component. We find that the Type 1 (unobscured) AGN do not enter the quiescent region of our proposed color space as they are too blue. Type 2 (obscured) AGN occupy a similar color space as DSFGs, which is unsurprising as Type 2 AGN tend to live in dust-obscured systems. Thus, AGN as an individual population are unlikely a primary contaminant in this color space, but instead may represent a contaminant subpopulation.

As shown in the Appendix, Figure A2 and predicted in Figure 1, heavily dust-obscured galaxies (with $A_V \geqslant 1$) lie primarily outside of the wedge due to their redder F277W – F444W colors. This is also illustrated by the colors of the 14 submillimeter sources identified via SCUBA-2 observations in the field (seen in our Figure 2; Zavala et al. 2017, 2018, 2022). Still, some contamination is expected since dust-reddened spectra can mimic the red colors of aged stellar populations. In the long (short) wedge, there are roughly 40 (22) objects with significant attenuation ($A_V \geqslant 1$) such that their potentially dust-reddened spectra pushes these objects into this color space. Nearly all (≳90%) of these dusty objects are predicted to sit at $z < 3$, though a handful have photo-z solutions at $z \sim 4$–5. Only one of the 14 DSFGs identified in Zavala et al. (2023) is captured in our wedge, demonstrating that the majority of potential dust-obscured contaminants may have low IR luminosities ($L_{\mathrm{IR}} \lesssim 10^{12}\ L_{\odot}$). This same object is deemed a quiescent galaxy by our SED photo-z fitting procedure, but we remove it from the final reported sample. Unfortunately, a more explicit quantification of this dust-obscured contamination rate requires additional data (e.g., the Atacama Large Millimeter/submillimeter Array (ALMA) or JWST) to fully confirm the nature of both the contaminants and the candidates.

Finally, we also find two galaxies with photo-z solutions at $z \sim 11$ within the wedge. Both of these objects have marginal or no detections blueward of the F150W band. One is also detected in Pérez-González et al. (2023) as a quiescent galaxy candidate at $z \sim 4$. Based on the discussion of redshifted SED templates, star-forming galaxies only enter this color space in specific redshift windows of $z \sim 3$–5 and $z \gtrsim 14$ due to emission lines for the former and significant Lyman breaks for the latter. This includes heavily dust-reddened spectra. Furthermore, the photo-z uncertainties on these objects are large ($\Delta z \sim 2$). Thus, we urge the reader to interpret the validity of these two contaminants with caution.

---

[33] https://ceers.github.io/LarsonSEDTemplates

[34] http://www.iasf-milano.inaf.it/~polletta/templates/swire_templates.html

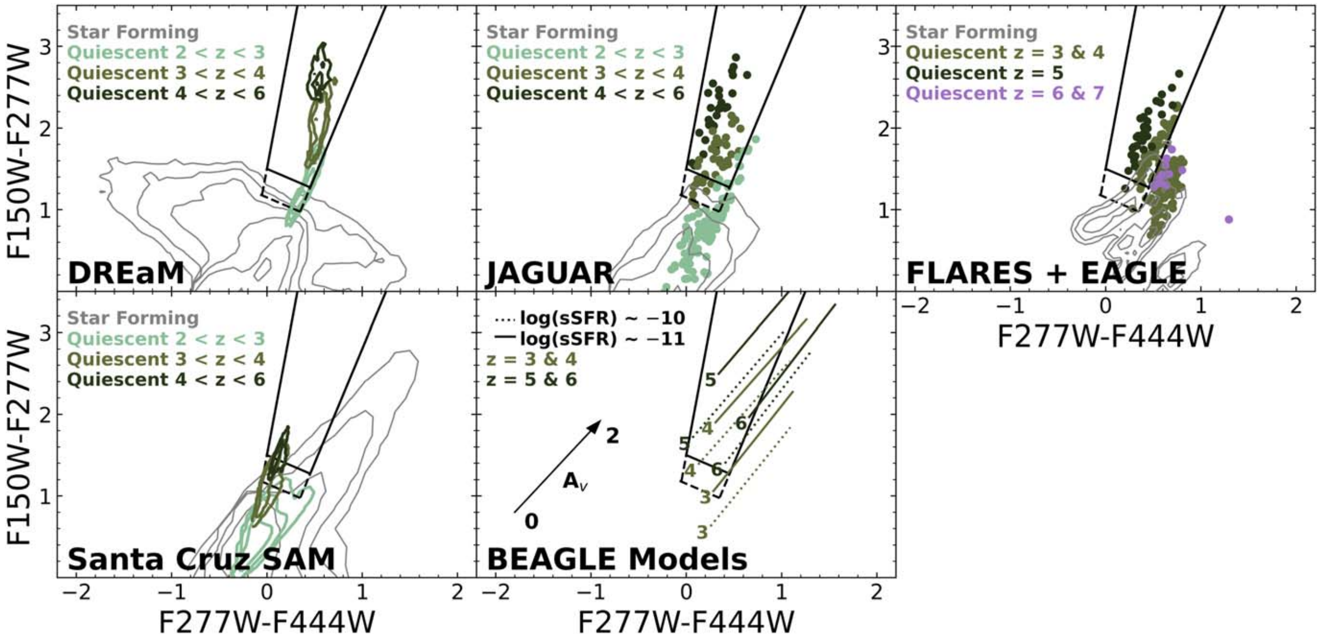

Figure 5. F277W − F444W vs. F150W − F277W colors for quiescent galaxies across several simulations. Black solid and dashed lines are the same "short" and "long" wedges denoted in previous figures. Top: mock galaxy colors from the DREaM semianalytical model (left, Drakos et al. 2022), the JAGUAR semianalytical model (middle, Williams et al. 2018), and the FLARES + EAGLE (right, Vijayan et al. 2021; Lovell et al. 2021, 2023) hydrodynamical simulations with quiescent populations highlighted in various shades of green and purple to mark their redshift ranges, with the remaining galaxies shown in gray contours. Bottom: mock galaxy colors from the Santa Cruz SAM (left, Yung et al. 2022) with a similar key as the figures in the top panel. On the right are mock galaxy colors generated by BEAGLE (Chevallard & Charlot 2016), same as in Figure 1. Details on how these colors are generated are presented in Section 2. Briefly, we show the color evolution of both aged (solid lines) and poststarburst (dotted lines) galaxies with varying levels of attenuation ($A_V = 0{-}2$) at $z = 3$, 4, 5, and 6.

5. Applied to Simulations

We apply the proposed color selection technique to a variety of cosmological simulations with mock JWST photometry, as shown in Figure 5. Our results can be used to compare the ability of various hydrodynamical simulations and semianalytic models to create sources that would be captured by our empirically derived selection approach. Specifically, we apply this color selection criteria to the Deep Realistic Extragalactic Model (DREaM) semianalytic model (Drakos et al. 2022), Santa Cruz semianalytic model (SAM; Somerville et al. 2015; Yung et al. 2019; Somerville et al. 2021; Yung et al. 2022), the JAdes extraGalactic Ultradeep Artificial Realizations phenomenological model (JAGUAR; Williams et al. 2018), and the EAGLE and FLARES hydrodynamical simulations (Vijayan et al. 2021; Lovell et al. 2021, 2023). We refer the readers to the references for details on these models and their assumptions.

Note that we apply the same definitions and requirements for high-z quiescent galaxy candidacy: objects must sit at $z \geqslant 2.5$ and exhibit sSFRs of $\log_{10}(\mathrm{sSFR/yr}) \lesssim -10$.

In general, $z \geqslant 3$ quiescent galaxy populations across the simulations are well captured by the long wedge. The empirical and semianalytic models (DREaM, JAGUAR, and Santa Cruz SAM) have simulated galaxy spectra that are fairly red due to perhaps their dust prescriptions or to the fact that they assign the SEDs of heavily evolved galaxies to their quiescent samples (e.g., Somerville et al. 2021); this is likely why the majority of high-z quiescent galaxies in these simulations fall neatly into the wedge space. Future work on how well this wedge captures young, poststarburst (i.e., bluer) quiescent galaxies will be needed. In the EAGLE and FLARES simulations, the main population missed by the wedge is $z \sim 3$ quiescent objects, which is in line with the BEAGLE model predictions (whether poststarburst or strongly evolved). Considering that the dominant contaminant population in all of these simulations is heavily dust-obscured galaxies (with $A_V \gtrsim 1$), and that each simulation has a unique prescription for dust production, attenuation, and/or extinction, it is clear that a better understanding of the prevalence of dust in both star-forming and quiescent galaxies is necessary. Such an analysis is beyond the scope of this paper and saved for future work.

6. Discussion and Summary

As mentioned in Section 3, our proposed color selection technique is not entirely distinct conceptually from several of the new rest-frame color selection techniques proposed in the literature. For example, when redshifted to $3 < z < 5$ the rest-frame synthetic $(ugi)_s$ filters explored in Antwi-Danso et al. (2023) constrain generally similar parts of the spectrum as the NIRCam F150W, F277W, and F444W bands proposed in this work (see also, e.g., Liu et al. 2018), which is likely why this technique yields the highest overlap with our candidate sources. The $NUV - U$ versus $V - J$ color diagram presented in Gould et al. (2023) is also similar at these redshifts, however the rest-frame J band at $z > 3$ presents a data challenge where MIRI observations are required to truly constrain this part of the spectrum. MIRI, with its smaller field of view and limited sensitivities, will not fully cover the NIRCam imaging for several of the early JWST legacy surveys currently underway. This is critical as quiescent galaxies at $z > 3$ are exceedingly rare ($n \sim 10^{-4}$–10^{-6} Mpc^{-3}; Girelli et al. 2019; Santini et al. 2019; Shahidi et al. 2020; Valentino et al. 2020; Carnall et al. 2023; Long et al. 2023), meaning that wide-field surveys with uniform multiband coverage are necessary to detect statistically significant samples of these objects. Lovell et al. (2023) also proposed observed-frame color selection diagnostics with JWST, however, both require MIRI photometry and are therefore currently limited to smaller data sets with these specific bands.

The strength of our proposed technique lies in its empirical nature, enabled by the filters on JWST's NIRCam instrument alone. With this technique, the initial labor in identifying these objects is significantly reduced: one does not need to generate photometric redshifts and/or SED catalogs for tens of thousands of objects as a prior step in the search for quiescent galaxies at $3 < z < 5$. Instead, it is clear from Figure 2 that red objects (whether quiescent or dust obscured) occupy a specific region in the F277W − F444W versus F150W − F277W color space, and that this can be exploited to identify a much smaller pool of candidates to pull from (i.e., <1% of all detected objects). Moreover, the candidate pool has known properties (i.e., dusty and/or quiescent), which provide distinct constraints on both SED fitting, and also follow-up observations for ruling out contaminants. This will undoubtedly increase our efficiency in discovering quiescent galaxies at high z.

Furthermore, this technique also shows potential for capturing more young, massive galaxies in the throes of quenching—i.e., poststarbursts—than most previously established techniques. Quiescent galaxies in the first 2 Gyr often have small, but significant amounts of UV light from their recent starburst episode (e.g., D'Eugenio et al. 2020a; Marsan et al. 2022). These slightly bluer colors are likely why many $z > 3$ quiescent galaxies can be missed in searches that use classic $z < 2$ quiescent galaxy selection techniques, as most are tuned to find red galaxies with no young stellar populations. As shown in Section 4, the average sSFR of newly discovered quiescent galaxy candidates in this work is roughly 5× (0.7 dex) lower than those that were also identified using canonical *UVJ* diagrams Williams et al. (2009), Carnall et al. (2023), and Valentino et al. (2023), as well as those captured by a *UVJ* color space modified to select younger, bluer candidates (Belli et al. 2019).[35] Therefore, this color plane demonstrates potential as a more complete selection method as it captures both mature and recently quenched massive galaxies at $z > 3$. However, larger samples are needed to explore and quantify its completeness at a statistical level.

Additionally, these results enable comparison between different cosmological simulations, each with their own physics prescriptions and initial assumptions. We find all simulations tested (DREaM, JAGUAR, FLARES + EAGLE, and Santa Cruz SAM) are able to produce some sources at $z \geqslant 3$ that are captured in the short and/or long wedges (Figure 5). However, the diversity in quiescent galaxy colors is broad across the simulations, and the nuances between initial assumptions and dust prescriptions in each simulation requires further work to understand how and why the differences in colors are so stark.

We use empirically constrained galaxy SEDs to derive an observed-frame color selection technique for massive quiescent galaxies at $3 \lesssim z \lesssim 5$ using JWST NIRCam imaging. Our F277W − F444W versus F150W − F277W color selection method is similar in concept to well-known color selection techniques in the literature (e.g., *UVJ*) but is more efficient and advantageous as it relies first on observed-frame colors to identify a candidate pool, over which then SED fitting can be performed, and also captures more young poststarburst galaxies than techniques tuned to the low-redshift Universe. We demonstrate the efficacy of this method by applying this technique to JWST imaging in the CEERS field: we identify 44 quiescent galaxy candidates at $2.5 < z < 6$. We recover nearly all quiescent galaxies at this epoch previously identified in the literature, and also discover 26 new candidates, the majority of which are likely poststarbursts. Similar to other color selection techniques, this technique also suffers from contamination from dust-obscured sources, though the quantification of this false-positive rate requires additional data (e.g., ALMA or JWST) to fully confirm the nature of both the contaminants and the candidates. Future, more refined versions of this technique will be developed upon the availability of additional wide-field observations with multiwavelength data (e.g., COSMOS-Web; Casey et al. 2023).

Acknowledgments

This work is dedicated to little Black girls whose hearts are set alight by scientific inquiry and exploration. May you live lives full of curiosity, and may the world never dull that light within you.

We honor the invaluable labor of the maintenance and clerical staff at our institutions, whose contributions make our scientific discoveries a reality. This work was developed and written in central Texas on the lands of the Tonkawa, Comanche, and Apache people.

A.S.L. would like to thank Charlie and Patrick Long for the love, support, and precious moments baking in the Sun together. A.S.L. would also like to thank Rachel Nere for her incisive curiosity surrounding JWST and galaxy evolution during the Summer 2022 TAURUS program. A.S.L. acknowledges support for this work provided by NASA through the NASA Hubble Fellowship Program grant #HST-HF2-51511.001-A, awarded by the Space Telescope Science Institute, which is operated by the Association of Universities for Research in Astronomy, Inc., for NASA, under contract NAS 5-26555.

This work is based [in part] on observations made with the NASA/ESA/CSA JWST. The data were obtained from the Mikulski Archive for Space Telescopes at the Space Telescope Science Institute, which is operated by the Association of Universities for Research in Astronomy, Inc., under NASA contract NAS 5-03127 for JWST. These observations are associated with program JWST #1345.

The CEERS NIRCam Images used in this article are available on the Mikulski Archive for Space Telescopes (MAST) at the Space Telescope Science Institute via doi:10.17909/z7p0-8481.

This work made use of Astropy,[36] a community-developed core Python package and an ecosystem of tools and resources for astronomy (Astropy Collaboration et al. 2013, 2018, 2022).

Appendix

In addition to the two wedges presented in this work, we also explored a wider wedge. This "red selection wedge" was explored as an option to capture potentially dust-reddened quiescent galaxies (see, e.g., the BEAGLE models presented in Figure 5). The red selection wedge has the same SNR requirements and uses the same three bands as the other

---

[35] However, as shown in Section 4.3.3, the majority of our sample is captured by the synthetic color space offered in Antwi-Danso et al. (2023), with no obvious biases toward younger or older populations.

[36] http://www.astropy.org

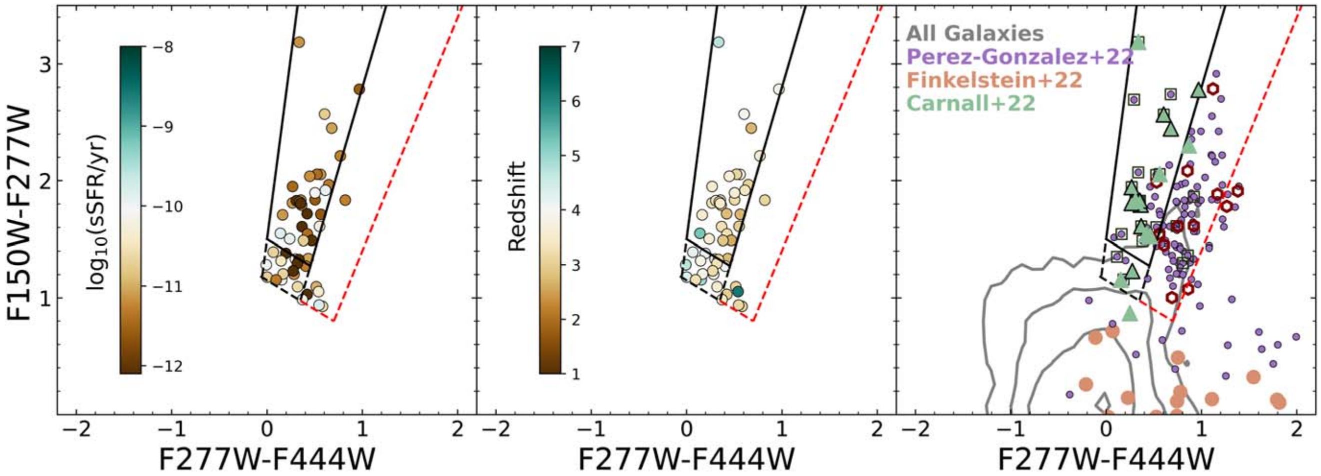

Figure A1. Same as Figure 2 in the main text, but here we show the additional handful ($n = 7$) of candidate $z \gtrsim 3$ quiescent galaxies recovered in the widened red wedge space. As shown in the following figure, the red wedge is heavily contaminated by dust-obscured galaxies, with diminishing returns on the identification of quiescent galaxies at high z.

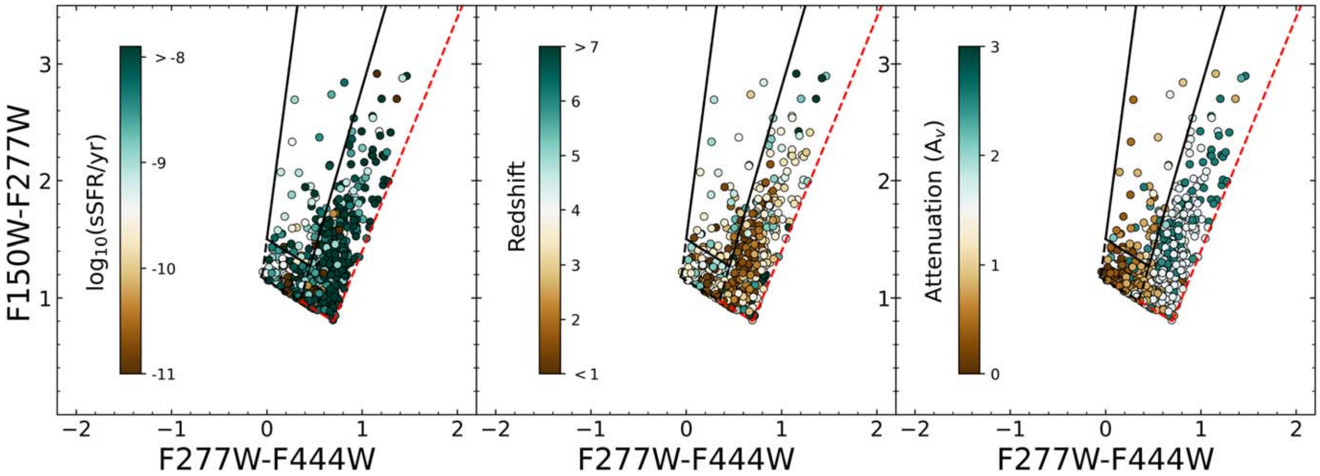

Figure A2. Same as the previous figure except here we show only the contaminants in each wedge. As expected from SED templates and existing literature studies in CEERS (e.g., Pérez-González et al. 2023), the wide/red wedge is occupied almost entirely by heavily dust-obscured galaxies with $A_V \geqslant 1$ at "Cosmic Noon" ($z = 1$–4).

wedges, but instead requires that galaxies meet the following criteria:

$$
\begin{aligned}
&\text{Red} - \text{A. } (\text{F150W} - \text{F277W}) < 1.5 + 6.25 \\
&\quad \times (\text{F277W} - \text{F444W}) \\
&\quad \text{and} \\
&\text{Red} - \text{B. } (\text{F150W} - \text{F277W}) > 1.15 - 0.5 \\
&\quad \times (\text{F277W} - \text{F444W}) \\
&\quad \text{and} \\
&\text{Red} - \text{C. } (\text{F150W} - \text{F277W}) > -0.6 + 2 \\
&\quad \times (\text{F277W} - \text{F444W}). \qquad \text{(A1)}
\end{aligned}
$$

The red selection wedge has the same Criterion A as the first two wedges presented in this work, the same Criterion B as the long wedge, and a new Criterion C which reaches redder into the F277W − F444W color space. The expansion of this wedge space is represented by the red dashed lines in Figures A1–A3.

Only seven additional $z \gtrsim 3$ quiescent galaxy candidates were recovered in this red wedge space, while the number of contaminants ballooned to an additional ∼500 sources, demonstrating the diminishing returns in widening the wedge to capture more red sources. As expected based on the empirically constrained SEDs in Figure 1 of the main text, the majority of these contaminants are fit as moderately to heavily obscured ($A_V \gtrsim 2$) star-forming galaxies at intermediate redshifts ($z \sim 1$–4). See Figure A2.

We also show this wide red wedge applied to simulations in Figure A3. The Santa Cruz SAM appears to model a significant population of red objects in this wider red wedge space that looks similar to the observations shown in Figure A1, but none are quiescent galaxies at $z \geqslant 3$. However, the EAGLE and FLARES simulations predict a population of quiescent galaxies at $z = 3$, 4, and 6 that would be best captured by the red wedge. Future discoveries, if any, of massive $z > 5$ quiescent galaxies will be useful in testing these color predictions.

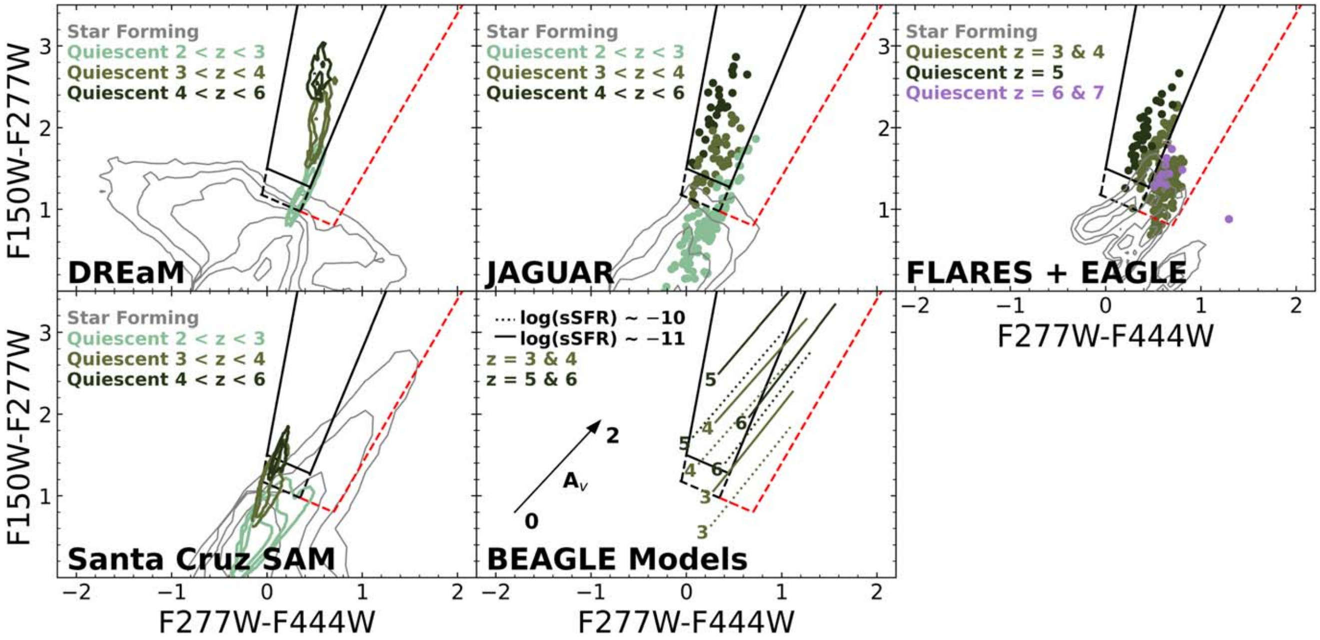

Figure A3. Same as Figures 1 and 5 except with the red wedge option overlaid in red dashed lines. The red wedge appears to capture $z \geqslant 3$ quiescent galaxies primarily in the EAGLE and FLARES simulations.

ORCID iDs

Arianna S. Long https://orcid.org/0000-0002-7530-8857
Jacqueline Antwi-Danso https://orcid.org/0000-0002-0243-6575
Erini L. Lambrides https://orcid.org/0000-0003-3216-7190
Christopher C. Lovell https://orcid.org/0000-0001-7964-5933
Alexander de la Vega https://orcid.org/0000-0002-6219-5558
Francesco Valentino https://orcid.org/0000-0001-6477-4011
Jorge A. Zavala https://orcid.org/0000-0002-7051-1100
Caitlin M. Casey https://orcid.org/0000-0002-0930-6466
Stephen M. Wilkins https://orcid.org/0000-0003-3903-6935
L. Y. Aaron Yung https://orcid.org/0000-0003-3466-035X
Pablo Arrabal Haro https://orcid.org/0000-0002-7959-8783
Micaela B. Bagley https://orcid.org/0000-0002-9921-9218
Laura Bisigello https://orcid.org/0000-0003-0492-4924
Katherine Chworowsky https://orcid.org/0000-0003-4922-0613
M. C. Cooper https://orcid.org/0000-0003-1371-6019
Olivia R. Cooper https://orcid.org/0000-0003-3881-1397
Asantha R. Cooray https://orcid.org/0000-0002-3892-0190
Darren Croton https://orcid.org/0000-0002-5009-512X
Mark Dickinson https://orcid.org/0000-0001-5414-5131
Steven L. Finkelstein https://orcid.org/0000-0001-8519-1130
Maximilien Franco https://orcid.org/0000-0002-3560-8599
Katriona M. L. Gould https://orcid.org/0000-0003-4196-5960
Michaela Hirschmann https://orcid.org/0000-0002-3301-3321
Taylor A. Hutchison https://orcid.org/0000-0001-6251-4988
Jeyhan S. Kartaltepe https://orcid.org/0000-0001-9187-3605
Dale D. Kocevski https://orcid.org/0000-0002-8360-3880
Anton M. Koekemoer https://orcid.org/0000-0002-6610-2048
Ray A. Lucas https://orcid.org/0000-0003-1581-7825
Jed McKinney https://orcid.org/0000-0002-6149-8178
Rachel Nere https://orcid.org/0009-0000-4358-5561
Casey Papovich https://orcid.org/0000-0001-7503-8482
Pablo G. Pérez-González https://orcid.org/0000-0003-4528-5639
Nor Pirzkal https://orcid.org/0000-0003-3382-5941
Paola Santini https://orcid.org/0000-0002-9334-8705

References

Antwi-Danso, J., Papovich, C., Leja, J., et al. 2023, ApJ, 943, 166
Astropy Collaboration, Robitaille, T. P., Tollerud, E. J., et al. 2013, A&A, 558, A33
Astropy Collaboration, Price-Whelan, A. M., Sipőcz, B. M., et al. 2018, AJ, 156, 123
Astropy Collaboration, Price-Whelan, A. M., Lim, P. L., et al. 2022, ApJ, 935, 167
Bagley, M. B., Finkelstein, S. L., Koekemoer, A. M., et al. 2023, ApJL, 946, L12
Belli, S., Newman, A. B., & Ellis, R. S. 2019, ApJ, 874, 17
Bertin, E., & Arnouts, S. 1996, A&AS, 117, 393
Boquien, M., Burgarella, D., Roehlly, Y., et al. 2019, A&A, 622, A103
Boylan-Kolchin, M. 2023, NatAs, 7, 731
Brammer, G. B., van Dokkum, P. G., & Coppi, P. 2008, ApJ, 686, 1503
Brammer, G. B., Whitaker, K. E., van Dokkum, P. G., et al. 2011, ApJ, 739, 24
Bruzual, G., & Charlot, S. 2003, MNRAS, 344, 1000
Bunker, A. J. & NIRSPEC Instrument Science Team 2020, in IAU Symp. 352, Uncovering Early Galaxy Evolution in the ALMA and JWST Era, ed. E. da Cunha et al. (Cambridge: Cambridge Univ. Press), 342
Burgarella, D., Buat, V., & Iglesias-Páramo, J. 2005, MNRAS, 360, 1413
Calzetti, D., Armus, L., Bohlin, R. C., et al. 2000, ApJ, 533, 682
Carnall, A. C., Walker, S., McLure, R. J., et al. 2020, MNRAS, 496, 695
Carnall, A. C., McLeod, D. J., McLure, R. J., et al. 2023, MNRAS, 520, 3974
Casey, C. M., Narayanan, D., & Cooray, A. 2014, PhR, 541, 45
Casey, C. M., Kartaltepe, J. S., Drakos, N. E., et al. 2023, ApJ, 954, 31
Cecchi, R., Bolzonella, M., Cimatti, A., & Girelli, G. 2019, ApJL, 880, L14
Chabrier, G. 2003, PASP, 115, 763
Chevallard, J., & Charlot, S. 2016, MNRAS, 462, 1415
Conroy, C., & Gunn, J. E. 2010, ApJ, 712, 833
da Cunha, E., Walter, F., Smail, I. R., et al. 2015, ApJ, 806, 110
Deshmukh, S., Caputi, K. I., Ashby, M. L. N., et al. 2018, ApJ, 864, 166
D'Eugenio, C., Daddi, E., Gobat, R., et al. 2020a, ApJL, 892, L2
D'Eugenio, F., van der Wel, A., Wu, P.-F., et al. 2020b, MNRAS, 497, 389
Drakos, N. E., Villasenor, B., Robertson, B. E., et al. 2022, ApJ, 926, 194
Dunlop, J. S., Abraham, R. G., Ashby, M. L. N., et al. 2021, PRIMER: Public Release IMaging for Extragalactic Research, JWST Proposal. Cycle 1, ID. #1837
Faber, S. 2011, The Cosmic Assembly Near-IR Deep Extragalactic Legacy Survey ("CANDELS"), STScI/MAST, doi:10.17909/T94S3X
Finkelstein, S. L., Dickinson, M., Ferguson, H. C., et al. 2017, The Cosmic Evolution Early Release Science (CEERS) Survey, JWST Proposal ID 1345
Finkelstein, S. L., Bagley, M. B., Ferguson, H. C., et al. 2023, ApJL, 946, L13
Forrest, B., Marsan, Z. C., Annunziatella, M., et al. 2020, ApJ, 903, 47

Girelli, G., Bolzonella, M., & Cimatti, A. 2019, A&A, 632, A80
Glazebrook, K., Schreiber, C., Labbé, I., et al. 2017, Natur, 544, 71
Gould, K. M. L., Brammer, G., Valentino, F., et al. 2023, AJ, 165, 248
Grogin, N. A., Kocevski, D. D., Faber, S. M., et al. 2011, ApJS, 197, 35
Hatziminaoglou, E., Pérez-Fournon, I., Polletta, M., et al. 2005, AJ, 129, 1198
Hwang, Y.-H., Wang, W.-H., Chang, Y.-Y., et al. 2021, ApJ, 913, 6
Jin, S., Sillassen, N. B., Magdis, G. E., et al. 2024, A&A, 983, L4
Koekemoer, A. M., Faber, S. M., Ferguson, H. C., et al. 2011, ApJS, 197, 36
Labbé, I., Huang, J., Franx, M., et al. 2005, ApJL, 624, L81
Labbé, I., Oesch, P. A., Bouwens, R. J., et al. 2013, ApJL, 777, L19
Larson, R. L., Hutchison, T. A., Bagley, M., et al. 2023, ApJ, 958, 141
Liu, F. S., Jia, M., Yesuf, H. M., et al. 2018, ApJ, 860, 60
Long, A. S., Casey, C. M., Lagos, C. d. P., et al. 2023, ApJ, 953, 11
Lovell, C. C., Harrison, I., Harikane, Y., Tacchella, S., & Wilkins, S. M. 2023, MNRAS, 518, 2511
Lovell, C. C., Vijayan, A. P., Thomas, P. A., et al. 2021, MNRAS, 500, 2127
Lovell, C. C., Roper, W., Vijayan, A. P., et al. 2023, MNRAS, 525, 5520
Marsan, Z. C., Muzzin, A., Marchesini, D., et al. 2022, ApJ, 924, 25
Martis, N. S., Marchesini, D. M., Muzzin, A., et al. 2019, ApJ, 882, 65
McKinney, J., Finnerty, L., Casey, C. M., et al. 2023, ApJL, 946, L39
Merlin, E., Fontana, A., Castellano, M., et al. 2018, MNRAS, 473, 2098
Merlin, E., Fortuni, F., Torelli, M., et al. 2019, MNRAS, 490, 3309
Muzzin, A., Marchesini, D., Stefanon, M., et al. 2013, ApJ, 777, 18
Nanayakkara, T., Glazebrook, K., Jacobs, C., et al. 2024, NatSR, 14, 3724
Noeske, K. G., Weiner, B. J., Faber, S. M., et al. 2007, ApJL, 660, L43
Noll, S., Burgarella, D., Giovannoli, E., et al. 2009, A&A, 507, 1793
Pacifici, C., Kassin, S. A., Weiner, B. J., et al. 2016, ApJ, 832, 79
Park, M., Belli, S., Conroy, C., et al. 2023, ApJ, 953, 119
Pérez-González, P. G., Barro, G., Annunziatella, M., et al. 2023, ApJL, 946, L16
Planck Collaboration, Ade, P. A. R., Aghanim, N., et al. 2016, A&A, 594, A13
Robertson, B. E., Tacchella, S., Johnson, B. D., et al. 2023, NatAs, 7, 611
Rodighiero, G., Bisigello, L., Iani, E., et al. 2023, MNRAS, 518, L19
Santini, P., Merlin, E., Fontana, A., et al. 2019, MNRAS, 486, 560
Schreiber, C., Glazebrook, K., Nanayakkara, T., et al. 2018, A&A, 618, A85
Shahidi, A., Mobasher, B., Nayyeri, H., et al. 2020, ApJ, 897, 44
Simpson, J. M., Swinbank, A. M., Smail, I., et al. 2014, ApJ, 788, 125
Smit, R., Bouwens, R. J., Labbé, I., et al. 2016, ApJ, 833, 254
Somerville, R. S., Popping, G., & Trager, S. C. 2015, MNRAS, 453, 4337
Somerville, R. S., Olsen, C., Yung, L. Y. A., et al. 2021, MNRAS, 502, 4858
Speagle, J. S., Steinhardt, C. L., Capak, P. L., & Silverman, J. D. 2014, ApJS, 214, 15
Steinhardt, C. L., Capak, P., Masters, D., & Speagle, J. S. 2016, ApJ, 824, 21
Stevans, M. L., Finkelstein, S. L., Kawinwanichakij, L., et al. 2021, ApJ, 921, 58
Straatman, C. M. S., Labbé, I., Spitler, L. R., et al. 2014, ApJL, 783, L14
Straatman, C. M. S., Spitler, L. R., Quadri, R. F., et al. 2016, ApJ, 830, 51
Tanaka, M., Onodera, M., Shimakawa, R., et al. 2023, arXiv:2311.11569
Toft, S., Smolčić, V., Magnelli, B., et al. 2014, ApJ, 782, 68
Valentino, F., Tanaka, M., Davidzon, I., et al. 2020, ApJ, 889, 93
Valentino, F., Brammer, G., Gould, K. M. L., et al. 2023, ApJ, 947, 20
Vijayan, A. P., Lovell, C. C., Wilkins, S. M., et al. 2021, MNRAS, 501, 3289
Weaver, J. R., Kauffmann, O. B., Ilbert, O., et al. 2022, ApJS, 258, 11
Whitaker, K. E., Labbé, I., van Dokkum, P. G., et al. 2011, ApJ, 735, 86
Williams, C. C., Curtis-Lake, E., Hainline, K. N., et al. 2018, ApJS, 236, 33
Williams, C. C., Oesch, P., Barrufet, L., et al. 2021, PANORAMIC—A Pure Parallel Wide Area Legacy Imaging Survey at 1-5 Micron, JWST Proposal. Cycle 1, ID. #2514
Williams, R. J., Quadri, R. F., Franx, M., van Dokkum, P., & Labbé, I. 2009, ApJ, 691, 1879
Wu, P.-F., van der Wel, A., Bezanson, R., et al. 2018, ApJ, 868, 37
Yung, L. Y. A., Somerville, R. S., Finkelstein, S. L., Popping, G., & Davé, R. 2019, MNRAS, 483, 2983
Yung, L. Y. A., Somerville, R. S., Ferguson, H. C., et al. 2022, MNRAS, 515, 5416
Zavala, J. A., Aretxaga, I., Geach, J. E., et al. 2017, MNRAS, 464, 3369
Zavala, J. A., Aretxaga, I., Dunlop, J. S., et al. 2018, MNRAS, 475, 5585
Zavala, J. A., Casey, C. M., Spilker, J., et al. 2022, ApJ, 933, 242
Zavala, J. A., Buat, V., Casey, C. M., et al. 2023, ApJL, 943, L9